Astroparticle Physics 125 (2021) 102510

Contents lists available at ScienceDirect

Astroparticle Physics

journal homepage: www.elsevier.com/locate/astropartphys

Resolving the tension in particle discrimination between the Simple and Picasso dark matter projects

T.A. Girard*, T.A. Morlat, A. Kling, M. Felizardo, A.C. Fernandes, J.G. Marques

Centro de Ciências e Tecnologias Nucleares, Instituto Superior Técnico, Universidade de Lisboa, 2695-066 Bobadela, Portugal

ARTICLE INFO

Article history:
Received 16 September 2019
Revised 27 July 2020
Accepted 28 August 2020
Available online 2 September 2020

Keywords:
Superheated liquids
Particle discrimination
Dark matter

ABSTRACT

We re-examine the longstanding disagreement between the SIMPLE and PICASSO superheated liquid-based dark matter search projects regarding discrimination between neutron- and α-induced bubble nucleation events, and its dependence on the distribution of liquid droplet sizes. A simple analysis based on (1) the interaction of α and neutrons with the detector droplet size distribution, combined with (2) the acoustics of the subsequent bubble expansion, reproduces the observations of each experiment under the reported measurement conditions. The differences in discrimination efficiency between the two experiments are shown to result from the relation between the droplet size distributions and the minimum α penetration distances in the liquid necessary to achieve the critical linear energy transfer necessary for bubble nucleation, the number of proto-bubbles generated in the transfer, and the subsequent bubble evolution. The results remove the tension between the SIMPLE and PICASSO experiments with respect to particle discrimination.

© 2020 Elsevier B.V. All rights reserved.

1. Introduction

All direct searches for astroparticle dark matter are critically dependent upon their ability to isolate WIMP-generated nuclear recoil events registered by the detector. Generally, this requires a significant attention to experimental background (both intrinsic and extrinsic) suppression, and a detector capable of distinguishing those that remain from the nuclear recoil events. Among the various detector types employed in such searches are superheated liquid devices, either superheated droplet detectors (SDDs) or bulk liquid bubble chambers. Our focus here is on the SDDs, with which there have been two search projects: SIMPLE and PICASSO.

In 2014, SIMPLE published a final report of its Phase II results [1], which achieved a spin-dependent exclusion contour minimum of 4.3×10^{-3} pb at 35 GeV/c^2 with 18.2 kgd exposure. The report included a simplified description of its droplet size distribution (DSD)-dependent particle response. In 2017 SIMPLE further reported on a series of experiments with small diameter droplets using the same description which again demonstrated the dependence of the SDD acoustic response [2] on the DSD.

In the same year, PICASSO presented its final, 345 kgd results [3], including the previous 140 kgd exposure [4], in which a contour minimum of 1.3×10^{-2} pb at 20 GeV/c^2 was achieved – a factor 3 less sensitive than SIMPLE with a factor 13 larger exposure. It further stated a lack of dependence of the particle-generated event responses on their DSD, challenging the SIMPLE particle discrimination and its reported efficiency of more than 97%. The statement itself is not consistent with the basic acoustic physics of the bubble evolution, and no accompanying elaboration of the statement was presented. The statement is however also found in an earlier Ref. [5], and an experimental justification provided in the earlier Ref. [6] via a series of dedicated experiments which did not reproduce the results of SIMPLE.

Both search experiments have since evolved to bubble chambers, leaving the disagreement unresolved. Given the impact of detector response and particle discrimination on potential SDD use, in astroparticle or other applications, we here elaborate on the model presented in Ref. [2], extending its description to include α-emissions both internal and external to the droplets, and elaborating on the acoustics of droplet expansion following proto-bubble nucleation.

The paper is divided into two principal sections. Section 2 summarizes the proto-bubble nucleation physics, and develops a geometric probability model which combines the nucleation conditions with the energy deposition of incident particles, in particular those of α decay at arbitrary locations with respect to the droplet. Section 3 describes the physics of the subsequent bubble expansion at the expense of the droplet liquid, and the associated acoustics of the expansion which explicitly defines the dependence of the acoustic signal on the DSD. The considerations of Sections 2 and 3 are combined in Section 4 to form a simple re-

---

[*] Corresponding author.
E-mail address: tagirard@ctn.tecnico.ulisboa.pt (T.A. Girard).

https://doi.org/10.1016/j.astropartphys.2020.102510
0927-6505/© 2020 Elsevier B.V. All rights reserved.

Table 1
Thermophysical properties of C_2ClF_5 (SIMPLE) at 9ºC and 2 bar, and C_4F_{10} (PICASSO) at 40ºC and 1 bar [11, 12].

Liquid	T/P [ºC/bar]	T_c [K]	T_b [K]	ρ_ℓ [kg/m^3]	ρ_v [kg/m^3]	$h_{\ell v}$ [kJ/kg]	σ [N/m]	ΔP [Pa]	r_{c0} [μm]	E_c [keV]
C_2ClF_5	9 / 2	353	251	1358	54.6	103	6.4×10^{-3}	3.8×10^5	3.4×10^{-2}	8.7
C_4F_{10}	40 / 1	386	271	1432	45.3	80.9	6.1×10^{-3}	3.3×10^5	3.7×10^{-2}	8.2

sponse model, which is applied to each of the two experiments with the results reproducing the published observations well. Conclusions, drawn in Section 5, identify the respective DSDs, proto-bubble creation, and subsequent bubble evolution as the basis for the difference in particle discrimination.

2. Bubble nucleation and particle interactions

A SDD consists of a distribution of micron-sized superheated liquid droplets (r_d) dispersed in a gel medium. Following the classical "heat spike" model of Seitz [7], a particle incident in a droplet deposits energy via creation of ionization electrons which generate a localized, cylindrical high temperature region (the "heat spike"), the sudden vaporization of which produces a shock wave in the surrounding liquid. As the energy is transmitted from the thermalized region to the surrounding medium through shock propagation and heat conduction, the temperature and pressure of the fluid within the shock enclosure decrease to their critical values, and a vapor-liquid interface is formed which may generate a proto-bubble of submicron critical radius (r_c) if the pressure difference ($\Delta P = P_v - P_\ell$, with $v =$ vapor, $\ell =$ liquid) exceeds the surface tension (σ) of the bubble. If this is not achieved, the vapor-liquid interface collapses; if achieved, the proto-bubble continues expanding via evaporation of the remaining droplet liquid as the droplet transitions from a liquid to vapor state.

For the purpose of clarity in what follows, we now somewhat unconventionally re-define $r_c \to r_c(t)$, $r_d \to r_d(t)$, with r_{c0} and r_{d0} the pre-expansion quantities at $t = 0$, respectively.

2.1. Proto-bubble nucleation

Assuming that proto-bubble formation occurs prior to the diffusion of the deposited energy from the proto-bubble volume, the particle energy deposition (E) must be at least equal to a thermodynamically-defined critical energy (E_c),

$$E_c = 4\pi r_{c0}^2\left(\sigma - T\frac{\partial\sigma}{\partial T}\right) + \frac{4\pi}{3} r_{c0}^3 \rho_v h_{\ell v} - \frac{4\pi}{3} r_{c0}^3 \Delta P, \tag{1}$$

where $r_{c0} = 2\sigma(T)/\Delta P$, T is the SDD operating temperature, ρ_v is the vapor density, and $h_{\ell v}(T) = h_\ell - h_v$ is the heat of vaporization.

Moreover, the deposited linear energy density (dE/dx) must be at least equal to a critical linear energy transfer (LET_c) defined by

$$LET_c \equiv E_c/L_c, \tag{2}$$

where $L_c = \Lambda r_{c0}$ is the effective ionic energy deposition length, with Λ a liquid-dependent parameter originally assumed 2 (such that $L_c = 2r_{c0}$); more recent determinations of Λ generally range from 2 to 12.96 [8], with reported larger values for neutron-induced recoil above 1 MeV [9]. Studies with heavy ions indicate that Λ may also depend on the ion mass number, decreasing with number increase [10]. Despite the variations, it is constant for a liquid at a given T, ρ_ℓ . Table 1 displays relevant properties of the liquids employed by SIMPLE and PICASSO at their operating temperatures and pressures. As seen, these are similar for both, as also their r_{c0} and E_c; this is anticipated since both are halocarbons.

Displayed as a function of the reduced superheat $s = (T - T_b)/(T_c - T_b)$, with T_c, T_b the critical and boiling temperature of the liquid at a given pressure, respectively, both E_c and r_{c0} are seen to lie on single curves for SDDs based on different liquids [8]. This is not however the case for Λ when similarly displayed [13]. Whereas r_{c0} and E_c are well-defined thermodynamically, Λ is without concrete theoretical basis and is usually determined experimentally via irradiation calibration measurements.

Similar to E_c and r_{c0}, the response of SDDs to a given irradiation lie on a "universal" curve when displayed in s [8]. Detector sensitivity to γ's and electrons is seen for $s \geq 0.51$, increasing with increasing s and well above the moderately superheated SDDs used in dark matter searches. An intrinsic minimum ionizing particle sensitivity of $\sim 10^{-10}$ is demonstrated by γ and electron irradiations [14], and particle backgrounds are essentially reduced to neutron-generated target nuclear recoils and α/heavy ions from naturally-occurring radioactive contaminants. We focus on these, considering each in turn.

2.2. Neutron-generated recoils

Weakly interacting massive particles (WIMPs) of 10–1000 GeV/c^2 kinematically imply elastically-scattered nuclear recoils of 1–100 keV. The detector acceptance window definition generally derives from neutron response calibrations involving irradiations using (α,n) sources [1, 15] and/or mono-energetic neutron beams [16, 15]: elastic neutron scattering off the target nuclei can provide nuclear recoils in the same energy window, the maximum energy of a recoil ion of atomic number M being given by $E_{nr}^{M} = \varpi_M E_n$, where E_n is the incident neutron energy, and $\varpi_M = \frac{4m_n M}{(m_n + M)^2}$. Inelastic scattering may also generate nuclear recoils for neutron energies above E_c, but the contribution is reduced by neutron moderation in the SDD hydrogenous gel matrix which down-scatters the E_n to below the reaction threshold [17], and is neglected in the discussion hereafter. Also neglected are transmutation reactions with positive Q-value which may also provoke proto-bubble nucleation (but have cross sections several orders of magnitude smaller than those of elastic scattering).

The calibration signals in both experiments generally derive from fluorine recoils [15] on account of its generally higher stopping power. Fig. 1 display track-averaged Bragg curves for fluorine ions of $E_{nr}^{F} = 5$–100 keV in C_2ClF_5 and C_4F_{10} at the SIMPLE and PICASSO operating temperatures and pressures respectively, calculated using SRIM [18] and tabulated liquid thermophysical properties [11, 12]. The indicated LET_c are those reported by the two experiments in Refs. [1, 15] respectively. In C_2ClF_5 the LET_c is exceeded over distances of $\leq 0.4\,\mu$m, significantly below the smallest droplet sizes of SIMPLE and ~10x the Λr_{c0}. For C_4F_{10} , the profiles in Fig. 1(b) are generally similar to Fig. 1(a). The lighter carbon ions, with higher recoil energies from the same neutron scatterings, penetrate somewhat larger distances in the respective liquids. The higher E_{nr} of Am/Be-generated neutron recoil events, ranging up to 2.8 MeV with LET larger than LET_c, are capable of penetrating several microns.

2.3. Alpha decay

The α-response of SDDs has been explored [1, 3, 4, 15] with ^{241}Am ($E_\alpha = 5.4$ MeV), U_3O_8 ($E_\alpha = 4.2$, 4.7 MeV), and ^{226}Ra decay ($E_\alpha = 4.78$, 5.49, 6.12 and 7.69 MeV) [19]. The larger kinetic energy of the ^{4}He ion, relative to that of the target liquid neutron

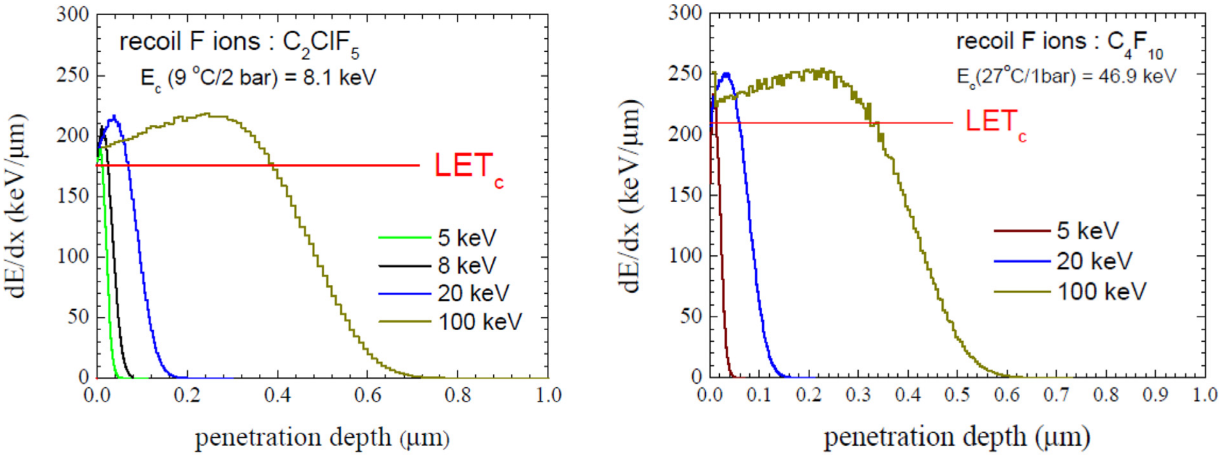

(a) (b)

Fig. 1. Bragg curves of recoil fluorine ions of various initial energies in (a) C_2ClF_5 at 9 °C/2 bar, and (b) in C_4F_{10} at 27 °C/1 bar.

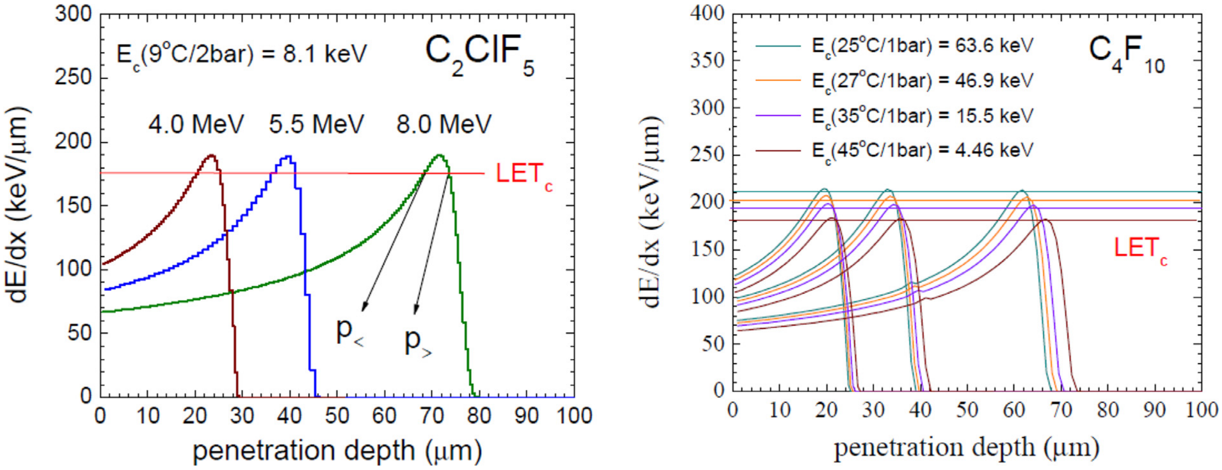

(a) (b)

Fig. 2. SRIM-computed Bragg curves for 4.0, 5.5 and 8.0 MeV α's in (a) C_2ClF_5 at 9ºC/2 bar; (b) C_4F_{10} at the indicated operating temperatures and 1 bar. The $p_<$, $p_>$ define the part of the α trajectory with dE/dx > LET_c.

recoils produces a significantly different Bragg curve relative to a target ion recoil, as a result of the M^{-1} dependence of the Bethe-Bloch equation [20] describing the dE/dx. This is shown in Fig. 2 for C_2ClF_5 and C_4F_{10} , calculated via SRIM for E_α representative of the U/Th decays at the experiments' operating temperatures and pressures; the indicated LET_c are again those reported in Refs. [1, 15]. In contrast to Fig. 1, the α's generally achieve LET larger than LET_c over distances of several microns in C_2ClF_5, *following* several tens of micron penetrations with LET less than LET_c; while similar in C_4F_{10}, the maximum of the Bragg peaks is virtually coincident with the LET_c at each temperature (again, following several tens of micron liquid penetration).

The majority of SDD α calibrations have employed actinide-doping, the ions of which have an electrochemical affinity for both the C_2ClF_5 and C_4F_{10} molecules [21, 22]. In this case, they preferentially populate the droplet surfaces; they also stabilize the emulsion by acting as a surfactant [21] since the ions are affinic to the hydrophobic surface of the droplets. The larger droplets consequently develop a higher bubble nucleation probability because of the increased surface-populations, and the 0-depth Bragg entries correspond to the droplet surfaces: droplets with diameters less than a minimum penetration depth $p_<$ (see Fig. 2(a)) do not support proto-bubble nucleation since the α transits the droplet without achieving LET_c; droplets with diameters greater than a penetration depth $p_>$ do not support further proto-bubble formation since the dE/dx is again less than LET_c.

In the case of non-actinide calibrations, the electrochemical affinity is absent [15] and the decay isotopes diffuse throughout the SDDs to populate both the droplets and gel. The proto-bubble nucleation probability depends on the droplet ability to contain the particle trajectory both below and above the LET_c; for decays external to the droplets, the probability depends on the energy loss in the gel prior to reaching a droplet.

The α decays are accompanied by decay daughter recoil ions (αr) with energies of 80 - 150 keV. As seen in their Bragg curves of Fig. 3 for $E_{\alpha r} = 100$ keV, these have penetration depths in C_2ClF_5 of ~ 0.10 µm, 0.08 µm of which is with LET greater than LET_c: the decay daughters behave more like the target ion recoils of Fig. 1(a) and will also mimic a WIMP-or neutron-generated recoil event if emitted within a droplet or near its surface.

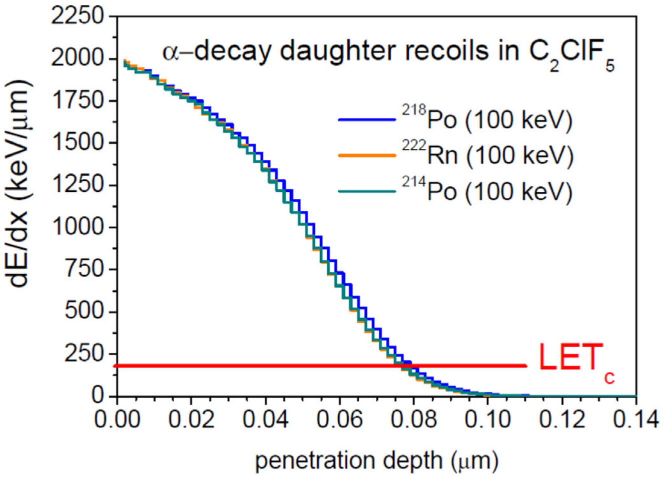

Fig. 3. SRIM-computed Bragg curves for representative α decay daughter nuclei in C_2ClF_5 at 9ºC/2 bar.

2.4. Geometric proto-bubble nucleation probabilities

Given the above, it is clear that different droplet sizes will respond differently under identical α-irradiation. We assume an effective event number $N_j^{eff}(r_{d0}) = P_j(r_{d0})\ N_d(r_{d0})$, with $j = (\text{nr}, \alpha, \alpha\text{r})$, $N_d(r_{d0})$ the DSD and $P_j(r_{d0})$ the j-th proto-bubble nucleation probability in a droplet of $\mathrm{r_{d0}}$.

For the neutron-generated nucleation probability, the acoustic response is experimentally seen [1] to overlap the DSD when scaled in terms of $\ln(r_{d0}^6)$ and shifted to overlap the respective distribution means. The first events are moreover seen to derive from the larger droplet sizes [1]: we adopt $P_{nr}(r_{d0}) = [\frac{r_{d0}}{r_{d0}^{\max}}]^3$such that the larger the droplet, the larger its probability of interaction.

The α probabilities are more involved owing to the required presence of the α-emitting material in the SDD. Since each α is accompanied by its decay daughter (αr) at 180º to the α, the α-droplet "interaction" then reduces to the geometric intersection of three spheres, two with coincident centers separated by a variable distance δ from the third of droplet radius r_{d0}: one is of radius $p_<$ (hereafter simply p_α), the second with radius $p_{\alpha r}$ as shown schematically in Fig. 4. The p_α are obtained from the intersection of the respective $\mathrm{LET_c}$ with the computed, density-dependent Bragg curve for the respective superheated liquid at its operating temperature/pressure and E_α, such as shown in Figs. 2 and 3.

To trigger bubble nucleation, the α must be emitted within the solid angle $\Omega = 2\pi(1\text{-}\cos\phi)$ defined by the r_{d0}-p_α sphere intersect. For the geometry of Fig. 4,

$$\cos\varphi(\delta, r_{d0}, p_j) = \left[\frac{1}{2p_j}\left\{\delta - (r_{d0}^2 - p_j^2)\delta^{-1}\right\}\right], \tag{3}$$

which when normalized to 4π provides a proto-bubble nucleation probability given by

$$\mathrm{P}_\Omega^{\mathrm{j}}(\delta, \mathrm{r_{d0}}, \mathrm{p_j}) = \frac{\Omega_j}{4\pi} = 1/2\left[1 - \frac{1}{2p_j}\left\{\delta - (r_{d0}^2 - p_j^2)\delta^{-1}\right\}\right], \tag{4}$$

with j restricted to α, αr. Note that in contrast to Refs. [2, 21] which examine the ratio of intersection-to-droplet volumes for the α only, Eq. (4) employs the ratio of Ω-to-4π of the p_j-sphere emission volume.

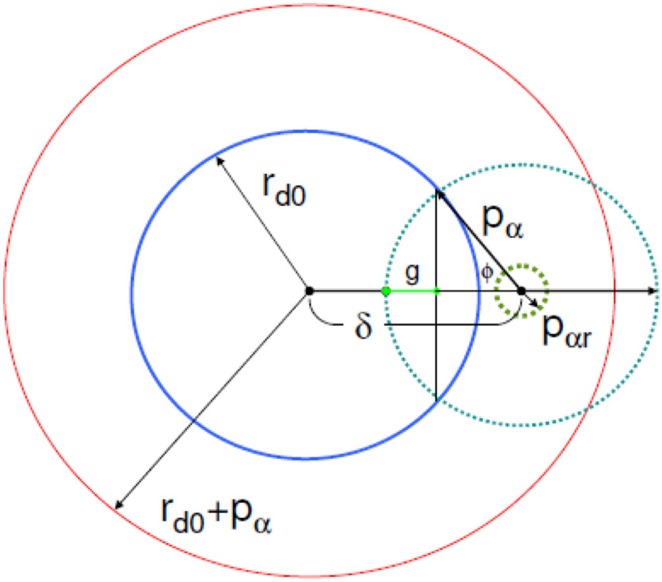

Fig. 4. droplet - α interaction model (not to scale). The droplet is represented by a sphere of radius $\mathrm{r_{d0}}$, the α-decay by two spheres of radius p_α and $p_{\alpha r}$ with coincident origins between $\delta = 0$ and R_α , where $R_\alpha = r_{d0} + p_\alpha$ is the "event horizon" since α's emitted beyond cannot reach the droplet with sufficient dE/dx to trigger a nucleation event. For $\delta > r_{d0}$, the p_α and $p_{\alpha r}$ are determined from the gel Bragg curves. The angle ϕ between p_α and δ is defined by $\cos\phi = (p_\alpha - g)/p_\alpha$.

The behavior of Eq. (4) is divided into two regimes, $r_{d0}\langle\ p_\alpha$ and $r_{d0}\rangle\ p_\alpha$, delineated by $r_{d0} = p_\alpha$ (P_Ω^α is a straight line with slope $\frac{1}{4p_\alpha}$ decreasing from 0.5 at $\delta = 0$). We show this in Fig. 5 as a function of δ for a representative $p_\alpha = 40\ \mu$m and various droplet r_{d0}. For $r_{d0}\langle\ p_\alpha$, $P_\Omega^\alpha < 0$ until $\delta = p_\alpha$- r_{d0}, then increases to a maximum at $\delta = (p_\alpha^2 - r_{d0}^2)^{1/2}$, decreasing smoothly thereafter to zero at $\delta = R_\alpha$. Similarly for $r_{d0}\rangle\ p_\alpha$, $P_\Omega^\alpha > 1$ until $\delta = r_{d0}$ - p_α, then smoothly decreases to zero at $\delta = R_\alpha$.

For an arbitrary droplet radius and E_α, the situation can be further divided into three cases depending on the location of the α decay with respect to the droplet center, such that $P_\Omega^{j,k}(r_{d0}) \rightarrow P_j^k(r_{d0})$, with $k = $ INT ($\delta < r_{d0}$), SURF ($\delta = r_{d0}$), EXT ($\delta > r_{d0}$). An integrated bubble nucleation probability P_j^k for a given r_{d0} and E_α is obtained by integrating Eq. (4) over δ between its respective limits for each r_{d0} in the DSD and p_j, and normalizing to the number of 4π in the integration. We examine each in turn.

2.4.1. Internal emission

The case $\delta = 0$ is special: the three spheres being center-coincident, there is no intersect except at $r_{d0} = p_\alpha$. Either $r_{d0} < p_\alpha$ ($P_\alpha^{INT} \equiv 0$), or $r_{d0} > p_\alpha$ ($P_\alpha^{INT} \equiv 1$): the pdf is a Heaviside function at $r_{d0} = p_\alpha$. Otherwise, we have two cases:

$$P_j^{INT}(r_{d0} = p_i) = \frac{\int_0^{r_{d0}} P_\Omega^j d\delta}{\int_0^{r_{d0}} d\delta} = \left\{\begin{array}{l} \left\{\dfrac{0 + \int_{p_j - r_{d0}}^{r_{d0}} P_\Omega^j d\delta}{\int_0^{r_{d0}} d\delta}\right\}(r_{d0} < p_j) \\ \left\{\dfrac{(r_d - p_j)\int_{r_{d0} - p_j}^{r_{d0}} P_\Omega^j d\delta}{\int_0^{r_{d0}} d\delta}\right\}(r_{d0} > p_j) \end{array}\right. \tag{5}$$

where $P_\Omega^\alpha\langle\ 0$ are set to zero and $P_\Omega^\alpha\rangle\ 1$ are set to 1. For a given DSD, $P_j^{INT} = P_j^{r_{d0} < p_j} + P_j^{r_{d0} > p_j}$.

Fig. 6(a) displays results for P_α^{INT} with representative E_α spanning the range of naturally-occurring α emissions, with the p_α taken from α Bragg curves computed for C_2ClF_5 at 9ºC/2 bar and the $\mathrm{LET_c}$ obtained from its reported measurement in Ref. [1]. As seen, the P_α^{INT} rise continuously from p_α-r_{d0} to a maximum at the largest r_{d0}. For reference purposes, two Gaussian DSDs of the form $\mathrm{N_d}(<r_{d0}>, \Sigma)$ with $<r_{d0}>$ the mean of the distribution radii and $\Sigma = (\text{FWHM}/2\sqrt{2\ln 2})$ are also shown: one with the $\mathrm{N_d}(30\ \mu\text{m}, 7.5\ \mu\text{m})$ of SIMPLE [1], the other with the $\mathrm{N_d}(100\ \mu\text{m}, 32\ \mu\text{m})$ of PICASSO [3]. As seen, while the smaller, narrow DSD is sensitive to

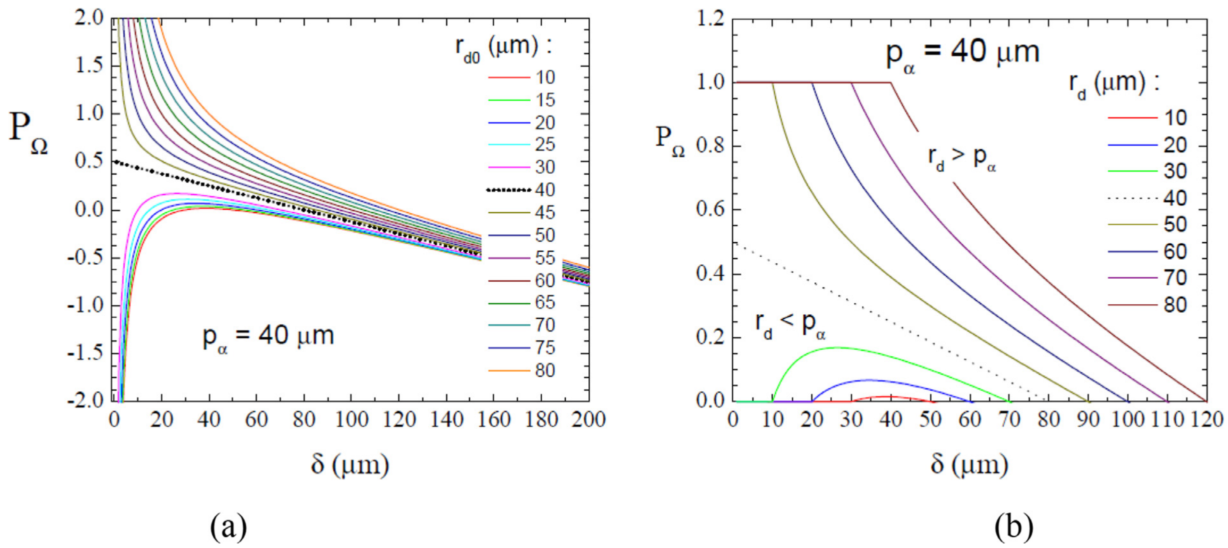

(a)

(b)

Fig. 5. (a) Eq. (4) for C_2ClF_5 at 9 ºC/2 bar, for $p_\alpha = 40$ μm and various r_{d0}; (b) same, but with $P_\Omega^\alpha \equiv 0$ for $r_{d0} \langle\ p_\alpha$ until $\delta = p_\alpha$ - r_{d0}, and $P_\Omega^\alpha \equiv 1$ for $r_{d0} \rangle\ p_\alpha$ until $\delta = r_{d0}$ - p_α.

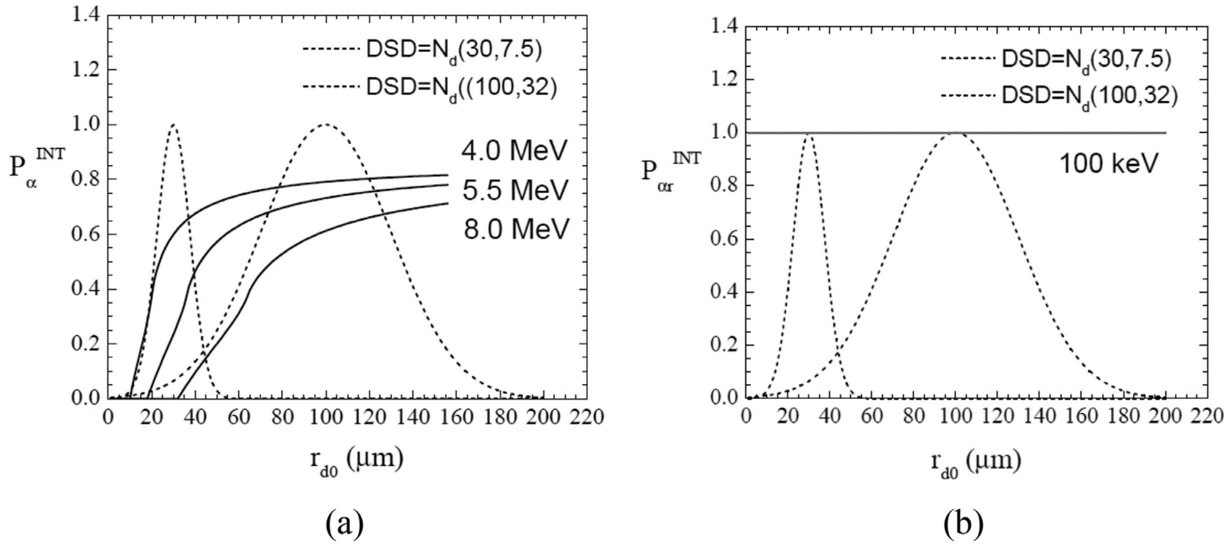

(a)

(b)

Fig. 6. variation of (a)P_α^{INT} with droplet radius for $E_\alpha = 4.0$, 5.5, and 8.0 MeV; (b) same for $P_{\alpha r}^{INT}$ with $E_{\alpha r} = 100$ keV. The dotted contours in black represent Gaussian DSDs of N_d(30 μm, 7.5 μm) and N_{d0}(100 μm, 32 μm).

$E_\alpha = 4.0$ MeV, the sensitivity decreases significantly with increasing E_α. The larger, broader DSD is in contrast generally sensitive to all E_α.

The $P_{\alpha r}^{INT}$ is similarly obtained by substitution of the daughter $p_{\alpha r}$, as shown in Fig. 6(b). In this case, all $r_{d0} > p_{\alpha r}$: $P_{\alpha r}^{INT} = 1$ for both reference DSDs, even if $P_\alpha^{INT} = 0$ since the αr is fully contained.

2.4.2. Surface emission

With droplet surface emission, $\delta = r_{d0}$ and Eq. (4) reduces to

$$P_j^{SURF} = \frac{1}{2}\left[1 - \frac{p_j}{2r_{d0}}\right]. \tag{6}$$

Fig. 7 display the results for P_α^{SURF}, $P_{\alpha r}^{SURF}$ with the same representative E_α,$E_{\alpha r}$ as in Fig. 6, accompanied by the same reference DSDs. As evident in Fig. 7(a), the P_α^{SURF} rise from $r_{d0} = p_\alpha/2$ to asymptotically approach a maximum ∼ 0.5 at the largest r_{d0}: the SDD is insensitive to α's if $r_{d0} < p_\alpha/2$, and higher energy α detection requires larger DSDs. For DSDs, the probability samples only the $2r_{d0} > p_\alpha$ tail, yielding few event asymmetric distributions which become increasingly symmetric as the DSD increases. As p_α increases with E_α, the sensitivity of small DSDs to higher E_α decreases.

Substituting $p_{\alpha r}$ for p_α, the contribution of the α recoils is 50% for all r_{d0}, as seen in Fig. 7(b), corresponding to half the daughter emission being into the half-space external to the droplet.

2.4.3. External emission

Bubble nucleation may also arise from α-emitters external to the droplet and within R_α. This case can also be treated by the analysis, but is complicated by the α trajectory being first in the gel and next in the liquid: in principle, the Bragg curve is computed for each gel track length within the cone of $\phi = 0$ - $\phi_{\max}$ defined by the r_{d0} - p_{gel} intersect; the curve is then integrated over δ, and the energy at the liquid interface computed, which is then used in a new Bragg construction to obtain the liquid p_j, and the P_j^{EXT} calculated to obtain the N_j^{eff}.

The range of the representative α Bragg peaks in glycerol (principal SIMPLE gel component) at 9 ºC/2 bar is reduced by ∼ 25% relative to C_2ClF_5 in Fig. 2(a). For illustrative purposes, we here use

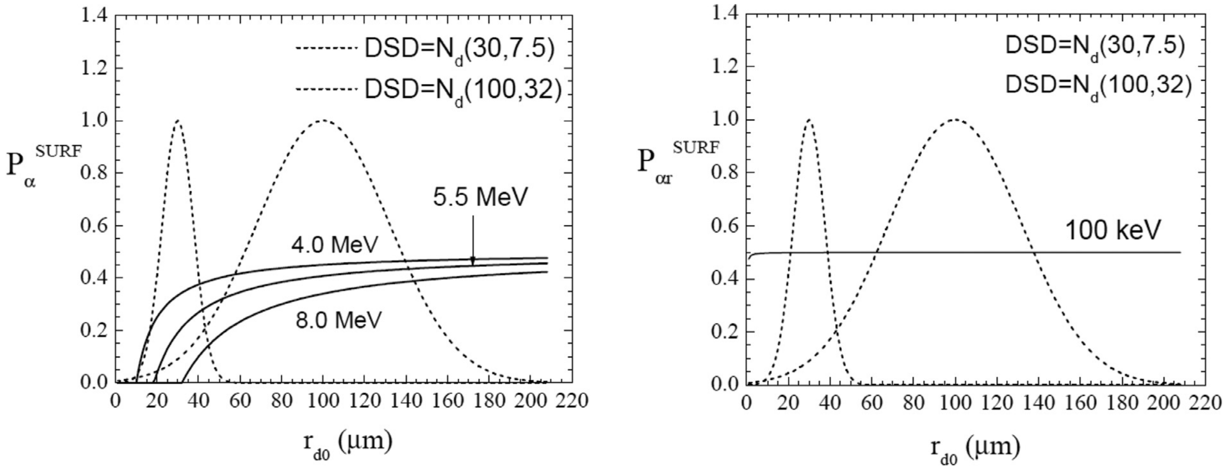

(a) (b)

Fig. 7. Variation of (a) $P_\alpha^{SURF}$with droplet radius for $E_\alpha = 4.0$, 5.5 and 8.0 MeV; (b) same for $P_{\alpha r}^{SURF}$ with $E_{\alpha r}=$ 100 keV. The dotted DSDs in black are the same as in Fig. 6.

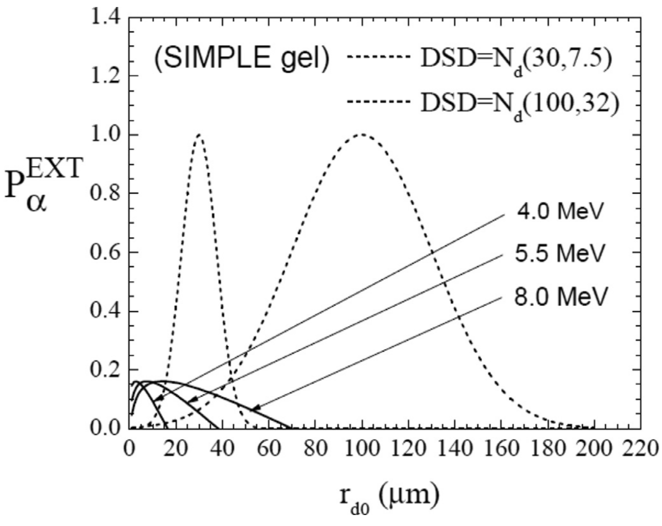

Fig. 8. variation of P_α^{EXT} with droplet radius for $E_\alpha = 4.0$, 5.5 and 8.0 MeV assuming the Bragg curves in the gel and liquid are similar. The dotted DSDs in black are the same as in Figs. 6 and 7.

the SIMPLE gel for the Bragg curve computations such that:

$$P_j^{EXT}\left(r_{d0}p_j\right) = \frac{\int\limits_{r_{d0}+0.1}^{R_\alpha} P_\Omega^j d\delta}{\int\limits_{r_{d0}+0.1}^{R_\alpha} d\delta} = \left\{ \begin{array}{l} \left\{ \frac{\int\limits_{r_d+0.1}^{p_j/2} P_\Omega^j d\delta + \int\limits_{p_j/2}^{R_\alpha} P_\Omega^j d\delta}{\int\limits_{r_{d0}+0.1}^{R_\alpha} d\delta} \right\} \left(r_{d0} < p_j\right) \\ \left\{ \frac{\int\limits_{r_{d0}+0.1}^{R_\alpha} P_\Omega^j d\delta \int_{r_{d0}+0.1}^{R_\alpha} P_\Omega^j d\delta}{\int\limits_{r_{d0}+0.1}^{R_\alpha} d\delta} \right\} \left(r_{d0} > p_j\right) \end{array} \right. \tag{7}$$

since the liquid and gel are density-matched ($\rho_{gel} \sim \rho_\ell$) in order to inhibit droplet sedimentation [23],

Fig. 8 provides the results for the representative E_α, again with the above reference DSDs; the corresponding display for $P_{\alpha r}^{EXT}$ is omitted since the α decay occurs beyond r_{d0}+0.1 and the α recoils are unable to reach the droplets. The P_α^{EXT} rises rapidly to a maximum of ~ 0.15 then smoothly decreases with decreasing Ω as δ increases with r_{d0}. Similar to Fig. 6(b) for αr, both distributions are sensitive to all three E_α. The sensitivity to external α emitters of small droplets is to those emitted at near-r_{d0} distances, eliminating the small droplet cutoffs of Fig. 6(a). The αr must be emitted from within the thin r_{d0} - to - r_{d0}+ 0.1μm shell outside the droplet, hence do not contribute.

2.4.4. Weighting factors

Each of the above P_α^k requires a weighting with respect to the number density of α emitters within the respective integration volumes V^k. This depends on whether the calibration was via actinide or non-actinide radio-isotopes. We define ω^ksuch that $N_\alpha^{eff} = \sum\limits_k \omega^k P_\alpha^k N_d$ with $\omega^k = f_k \frac{V^k}{V_{R_\alpha}}$ and $f_k = \frac{N_\alpha^k}{V^k}$ is the fraction of V^koccupied by emission sites. For the actinides, we assume the decay nuclei to be located in a thin shell (r_{d0}-to-r_{d0}+0.1 μm) at the droplet surface, such that $\omega^{INT} = \omega^{EXT} = 0$, and $\omega^{SURF} = f_{SURF}\frac{V^{SURF}}{V_{R_\alpha}}$. For the non-actinide,

$$\begin{aligned} \omega^{INT} &= f_{INT}\frac{{r_{d0}}^3}{R_\alpha^3}, \\ \omega^{SURF} &= f_{SURF}\frac{\left[(r_{d0}+0.1)^3 - r_{d0}^3\right]}{R_\alpha^3}, \\ \omega^{EXT} &= f_{EXT}\frac{(R_\alpha^3 - r_{d0}^3)}{R_\alpha^3}. \end{aligned} \tag{8}$$

The density of the α emission sites however may not be uniform between the V^k [15], in which case $f_k = f_k(\delta)$ and the weighting requires inclusion in each of the integrations. In the absence of sufficient information, and for simplicity, we assume a uniform distribution of emission sites: Fig. 9 show the impact of the weighting on the P_α^{INT} and P_α^{EXT} of Figs. 6 and 8, respectively, with $f_k = 1$: the contours are now reduced and ordered in E_α, as anticipated from the differing p_α.

3. Proto-bubble / droplet evolution and acoustics

If a dynamically stable proto-bubble is achieved, it continues to expand by evaporation of the remaining droplet liquid, displacing the liquid as the droplet transitions from a liquid to vapor state.

3.1. Proto-bubble evolution

The growth of the proto-bubble is initially limited only by the inertia of the surrounding liquid, as described by Rayleigh-Plesset [24] :

$$\Delta P = \frac{3}{2}\rho_\ell\left(\frac{dr_c}{dt}\right)^2 + \rho_\ell r_c\frac{d^2 r_c}{dt^2}. \tag{9}$$

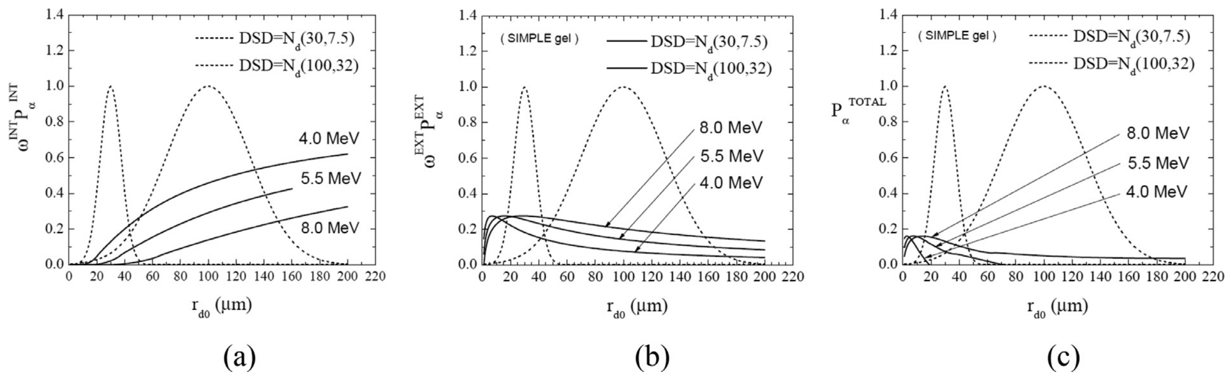

(a) (b) (c)

Fig. 9. variation of (a) $\omega^{\rm INT}P_\alpha^{EXT}$ and (b) $\omega^{\rm EXT}P_\alpha^{EXT}$ with droplet radius for $E_\alpha = 4.0$, 5.5 and 8.0 MeV; (c) variation of P_α^{TOTAL} with droplet radius for $E_\alpha = 4.0$, 5.5 and 8.0 MeV. The dotted DSDs in black are the same as in Figs. 6–8.

Table 2
Thermodynamic properties of C_2ClF_5 and C_4F_{10} at T_S [33].

Liquid	ρ_ℓ^* [kg/m^3]	ρ_v^* [kg/m^3]	c_p^* [kJ/kg K]	$h_{\ell v}^*$ [kJ/kg]	D_ℓ^* [m^2/s]
C_2ClF_5(2 bar)	1488	16.0	0.966	119	1.16×10^{-6}
C_4F_{10} (1 bar)	1593	11.2	1.028	96.7	1.32×10^{-6}

The solution assuming a negligible surface tension is $r_c^{inertial}(t) = \psi_{\rm inertial}$ t, with

$$\psi_{\rm inertial} = \left(\frac{2}{3\rho_\ell}\Delta P\right)^{1/2}. \tag{10}$$

The bubble grows with constant velocity at the expense of energy stored in the droplet liquid itself, which is several orders of magnitude greater than the total energy lost by a 5 MeV α.

As bubble growth progresses, evaporation cools the liquid-vapor interface to a saturated state, and growth slows with temperature/pressure decrease via heat conduction and viscosity losses: increasing amounts of heat transfer to the interface are required. This "thermal stage" is determined entirely by the bulk liquid thermodynamics, and described by Plesset-Zwick [25] by

$$\frac{\partial T}{\partial t} + \rho_\ell \frac{r_c^2}{R^2}\frac{\partial r_c}{\partial t}\frac{\partial T}{\partial R} = D_\ell\left(\frac{\partial^2 T}{\partial R^2} + \frac{2}{R}\frac{\partial T}{\partial R}\right), \tag{11}$$

with T the liquid temperature at a distance R from the droplet, and D_ℓ is the thermal diffusivity of the liquid in the saturated state. The solution, assuming a thin thermal boundary layer at the bubble-liquid interface, is $r_c^{thermal}(t) = \psi_{thermal}$ $t^{1/2}$ [26, 27], for which the leading order approximation is generally

$$\psi_{\rm thermal} = \Gamma J_a^* (D_\ell^*)^{1/2}, \tag{12}$$

where J_a is the Jacob number given by

$$J_a^* = \frac{\rho_\ell^* c_p^* \Delta T^*}{\rho_v^* h_{\ell v}^*}, \tag{13}$$

with * denoting thermodynamic parameters at the liquid saturation temperature (T_S); c_p is the liquid specific heat at constant pressure, $\Delta T = T - T_s$, and the pre-factor Γ varies with the specific treatment of Eq. (11) by various authors [25–32], from which we adopt $\Gamma = \sqrt{\frac{12}{\pi}}$ [32]. Table 2 provides relevant properties of C_2ClF_5 and C_4F_{10}, which again are seen not to differ significantly between the liquids.

The above solutions are asymptotic to the bubble growth: a complete description involves a smooth transition between the inertial and thermal stages, which is described [34, 35] in terms of scaled, dimensionless variables t^+ and R^+ from interpolation between the limiting solutions of Eqs. (9) and (11) for large and small times as $R^+ = 2/3\ [(t^+ + 1)^{3/2} - (t^+)^{3/2} - 1]$, as shown in Fig. 10. The scaled variables are given by

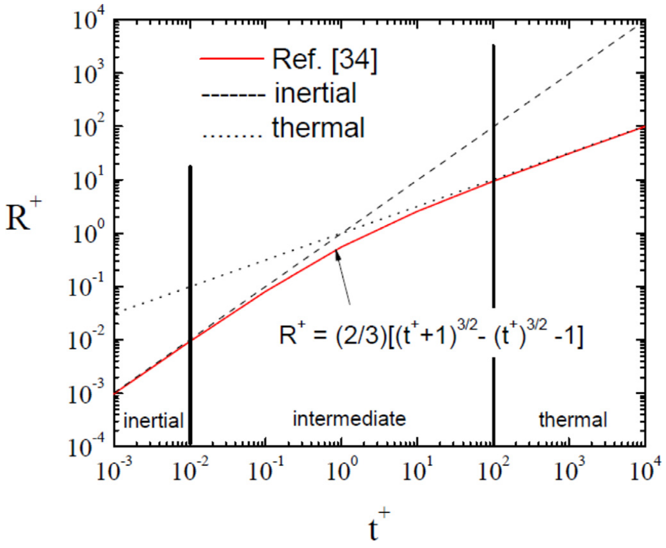

Fig. 10. overall proto-bubble expansion with time (adapted from [34]) in terms of dimensionless t^+, R^+ as defined in the text.

$$t = t^+\left(\frac{\Psi_{inertial}}{\Psi_{thermal}}\right)^{-2}$$

and

$$r_c = R^+\left(\frac{\Psi_{inertial}}{\Psi_{thermal}}\right)^{-2}\psi_{\rm inertial} \tag{14}$$

so that the Figure is "universal": once t^+ is determined from Eq. (14), R^+ can be read from Fig. 10 and Eq. (14) applied to obtain $r_c(t)$.

This is seen to generally agree with experiment for $J_a^* > 10$ but not below, since use of Eq. (12) confines the description to larger J_a^* where the thermal boundary layer assumption is valid [34].

3.2. Droplet evolution

As the growing proto-bubble $r_c(t)$ expands against the decreasing liquid, the remaining liquid shell itself expands against the gel.

The relation of the droplet intermediate state r_d(t) to the r_{d0} of the DSD is obtained by approximating each droplet with two concentric spheres of inner radius r_c(vapor) and outer radius r_d (vapor + remaining liquid), such that

$$r_d(\mathrm{t}) = \left[\mathrm{n_j}\left(1 - \left[\frac{\rho_v}{\rho_\ell}\right]\right)r_c^3 + r_{d0}^3\right]^{1/3} \tag{15}$$

where the evaporated liquid equivalent ($r_{c\ell}$) is obtained via mass conservation as $r_{c\ell}(t) = (\frac{\rho_v}{\rho_\ell})^{1/3} r_c(t)$. Eq. (15) moreover accounts for possible multi-proto-bubble generation as suggested in Fig. 2(a), each of which would serve as an evaporation center for the droplet: assuming that each evolves identically and independently, we replace t with $t = t_0/n_j$, where t_0 is the $n_{nr} = 1$ liquid evaporation time of a neutron-generated target recoil, and n_j is the number of proto-bubbles created by radiation type j.

A completed bubble evaporation occurs on a millisecond time scale, resulting in a vibrating bubble of $r_{df} = (\frac{\rho_\ell}{\rho_v})^{1/3} r_{d0}$ which oscillates around an equilibrium radius at ambient pressure, with a low frequency resonance ν_r given by [36]

$$\nu_r = \frac{1}{2\pi r_{df}}\sqrt{\frac{3\kappa P}{\rho_\ell}}, \tag{16}$$

where, κ is the polytropic vapor coefficient, and P is the ambient equilibrium pressure.

In summary, only on nanosecond time scales is an acoustic signal (shock wave) formed at the expense of the particle deposition energy; once the proto-bubble is formed, the droplet expansion depends on the thermodynamic properties of the liquid alone.

3.3. Acoustics

The droplet expansion r_d(t) is accompanied by an outgoing subsonic pressure wave, with the pressure generated at a distance R given by [29, 37, 38]

$$\delta P(R, r_d, t) \;= \frac{\rho_\ell}{4\pi R}\frac{d^2V(t - \frac{R}{c})}{dt^2} = \frac{\rho_\ell}{R}\left[\frac{d^2r_d}{dt^2}r_d^2 + 2r_d\left(\frac{dr_d}{dt}\right)^2\right], \tag{17}$$

where c is the speed of sound in the gel. The pressure is sensed by external microphones, converted to voltages and analyzed to provide the SDD signal in both experiments: the observable is the signal amplitude $\mathrm{A(t)} = \vartheta(\delta_\mathrm{P})$, with ϑ the microphone μV/μbar conversion.

Substituting the solutions of Eqs. (9) and (11) in Eq. (17) yields for either growth stage

$$\mathrm{A(r_d)} \;= \mathrm{A_m r_d^3 t^{-2}}, \tag{18}$$

where t is the time of droplet expansion, $m =$(inertial, thermal), and the parameters $A_{inertial} \;=\; \vartheta(\frac{2\rho_\ell}{R})$, $A_{thermal} \;=\; \vartheta(\frac{\rho_\ell}{4R})\cdot$are constants for a given detector and operating conditions.

The acoustic power radiated through a spherical surface at a distance R by the expanding droplet is given by $\mathrm{K}(r_d) = \frac{4\pi R^2 A^2}{Z}$, where $Z = c\rho_\ell$ is the acoustic impedance [39], such that

$$K_j(r_d(t), n_j) = A_m^2 r_d^6 n_j^4 \tag{19}$$

With the inclusion of multiple proto-bubble generation. As evident from the above, most of the acoustic power is emitted during the inertial stage. The associated acoustic energy is obtained by integrating Eq. (19) over the expansion time τ:

$$W_j(r_d(t), n_j) = \int_0^\tau K_j dt = 3^{-1} = A_m^2 r_d^6 n_j^3, \tag{20}$$

4. Response model and applications

The discrimination qualities of both experiments are generally presented as nucleation event numbers, normalized to the maximum of the respective acoustic distribution as a function of either ln(K) [1] or log(W) [3]. In model terms, the ordinate corresponds to$N_j^{eff} = \omega^\mathrm{k} P_j^k \mathrm{N_d}(r_{d0})$, the $\omega^\mathrm{k} P_j^k$determining which r_{d0} contribute to the signal, and by how much. The abscissa, in contrast, corresponds to a logarithm of the recorded A^2 of the associated acoustic signal of the droplet evolution.

The neutron mean free path is larger than any droplet diameter in either experiment: subsequent elastic scatterings occur in the gel or other droplets with few microsecond time separations. Assuming $n_{nr} = 1$ for the neutron-generated recoil events [1, 15], the ln(A_m^2) or log(A_m^2) of Eqs. (19) and (20), containing all constants of the measurement, can be treated as a “shift factor” for co-locating the mean of $N_{nr}^{eff}(r_{d0})$ with the experimental response mean. The $N_{\alpha+\alpha r}^{eff}(\mathrm{r_{d0}})$ is then calculated according to the nature of the α calibration, and the associated $K_{\alpha,\alpha r}$computed with $n_\alpha \;\geq\; 1$, $n_{\alpha r} = 1$, and shifted by the same amount to complete the spectrum.

4.1. Application : SIMPLE

The SIMPLE science SDDs employed 900 ml (10 cm Ø, 12 cm height) SDDs with C_2ClF_5 homogeneously dispersed in Gaussian DSDs of $\mathrm{N_d}(<r_{d0}>, \Sigma) = \mathrm{N_d}(30\,\mu\mathrm{m},\ 7.5\,\mu\mathrm{m})$ [1]. Neutron irradiations were performed with weak sources of Am/Be, or low energy, mono-energetic neutron beams [2, 16]. Alpha irradiations were made by doping the SDDs with a ^{241}Am solution during fabrication. Smaller 150 ml (8 cm Ø, 10 cm height) versions of the science SDD were made with the fabrication protocol scaled for detector volume to provide comparative results for the p_α of an U_3O_8 solution. All results were obtained at an operating temperature/pressure of 9ºC/2 bar.

SIMPLE used a single electret microphone (0.1–20 kHz) per detector, mounted within a glycerin layer covering the SDD emulsion, with sensitivity of $\vartheta = 7.9\times10^{-2}$ μV/μbar and no amplification [1]. The analysis was based on the maximum acoustic power of an event, displayed as $\mathrm{N_{events}}(r_{d0})$ vs. ln(K); as shown in Fig. 2 of Ref. [1], the results yielded a 30 mV gap between the neutron- and α-generated events, with a 0.3 mV resolution.

The signal corresponds to the end of the inertial stage (t_X), which is estimated from Fig. (10) and the solutions of Eqs. (14), (10), (12); the associated bubble radius $r_{cX} = \psi_{\mathrm{inertial}} \times t_X$. The results for C_2ClF_5 (9ºC/2 bar) are $t_X = 4.73\ \mu$s, $\Psi_{\mathrm{inertial}} = 13.7\,\mu\mathrm{m}/\mu$s, and $r_{cX} = 64.8\,\mu$m, in reasonable agreement with similar estimates in other liquids [25–30, 37, 38]. The evaporated liquid equivalent $r_{cX-\ell} = (\frac{\rho_v}{\rho_\ell})^{1/3} r_{cX} = 22.2\,\mu$m : for $r_{d0} \leq r_{cX-\ell}$, the droplet liquid is consumed; for $r_{d0} > r_{cX-\ell}$ however, the remaining liquid is contained in a shell surrounding the bubble, the thickness of which depends on the initial r_{d0}. Using Eq. (15), $r_{dX} = r_d(t = \mathrm{t_X})$ is then

$$\mathrm{r_{dX}} = \begin{cases} \mathrm{n_j}\left[\frac{\rho_\ell}{\rho_v}\right]^{1/3} \quad \mathrm{r_{d0}} \;\left(\mathrm{r_{d0}} \leq r_{cX-\ell}n_j^{1/3}\right) \\ \left[\mathrm{n_j}\left(1 - \left[\frac{\rho_v}{\rho_\ell}\right]\right)r_{cX}^3 + r_{d0}^3\right]^{1/3} \quad \left(r_{d0} > r_{cX-\ell}n_j^{1/3}\right) \end{cases} \tag{21}$$

Fig. 11 displays r_{dX} as a function of r_{d0} in the case n_j =1 for C_2ClF_5 at 9º C/2 bar.

As seen, $\mathrm{r_{dX}}$ increases linearly until $r_{cX-\ell}$, where it abruptly slows as a result of the redistribution of the remaining liquid within the increasingly larger shell.

We rewrite Eq. (19) using Eq. (21), $K_j(r_{dX}, n_j) = A_m^2 r_{dX}^6 n_j^4$ where all constant factors including t_X are now subsumed into A_m^2. A comparison of the results of the analysis with those of neutron irradiation response is shown in Fig. 12.

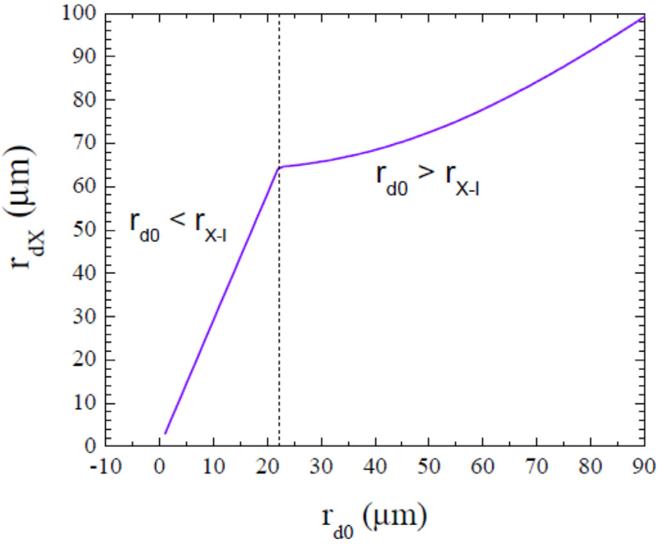

Fig. 11. variation of r_{dX} at the end of the inertial stage with respect to the initial droplet size.

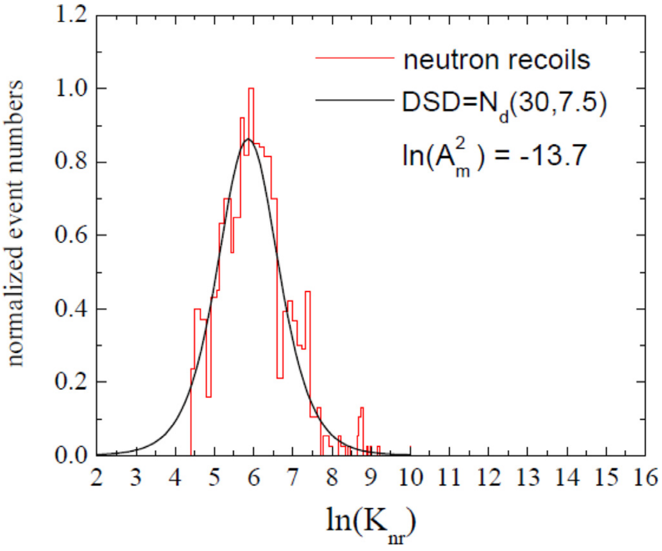

Fig. 12. comparison of the model neutron irradiation response with the results of SIMPLE SDD neutron irradiation. The sharp low acoustic power cutoff is the result of the microphone sensitivity.

4.1.1. Small droplets

For the U_3O_8 calibrations of the 150 ml SDDs with Gaussian DSD of $N_d(<r_d>,\Sigma) = N_d(11\,\mu m,\ 1.1\ \mu m)$, P_α^{TOTAL}equals P_α^{SURF} and p_α is 22 μm ($\sim r_{cX-\ell}$) from interpolation of Fig. 2(a). Note that$N_d(r_{dX}) \sim N_d(r_{d0})$ because of the small droplet sizes. The N_{nr}^{eff} is shifted by −6.9 to overlap the mean of the experimental $\ln(K_{nr})$ distribution (as in Fig. 12); the $N_{\alpha+\alpha r}^{eff}(r_{dX}) = 0.5[P_\alpha^{SURF} + P_{\alpha r}^{SURF}]N_d(r_{d0})$ is then calculated, $K_{\alpha,\alpha r}$ computed with $n_\alpha = 2$, $n_{\alpha r} = 1$, and then identically shifted, and n_α adjusted to reproduce the experimental result. The results with $n_\alpha = 1.8$, shown in Fig. 13(a), yield an asymmetric α response distribution promoted above the neutron recoil (nr) distribution in agreement with Fig. 9 of Ref. [1].

4.1.2. Large droplets

For the science results with a Gaussian DSD of N_d(30 μm, 7.5 μm), the α background likely derived from the glass containment U/Th contamination [17] and high radon concentration in the underground site at the time [1]. The decay chain is ^{222}Rn –($t_{1/2} = 3.8$ d)-> 5.59 MeV $\alpha + {}^{218}$Po –($t_{1/2} = 3$ min)-> 6.12 MeV $\alpha + {}^{214}$Pb –($t_{1/2} = 29$ min)-> $\beta + {}^{214}$Bi –($t_{1/2} = 20$ min)-> $\beta + {}^{214}$Po –($t_{1/2} = 0.16$ ms)-> 7.83 MeV $\alpha + {}^{210}$Pb [22]. At 9 ºC/2 bar, $E_c = 8$ keV and $LET_c = 176$ keV/μm: the SDD is sensitive to all decay chain α's and their αr daughters. Since $P_{\alpha r} \sim 1$, any internal decay will trigger a bubble nucleation, after which the droplet is no longer sensitive to subsequent decays. We assume the Rn to be the principal contributor, so that $E_\alpha = 5.6$ MeV, and $p_\alpha = 37$ μm from interpolation of Fig. 2(a). The N_{nr}^{eff} is shifted by −14.6 to overlap the experimental mean of $\ln(K_{nr})$, accounting for the $\ln(A_m^2)$. The $N_{\alpha+\alpha r}^{eff}$ for $\delta > r_{d0}$+0.1 μm$= [P_\alpha^{INT} + P_\alpha^{EXT}]N_d(r_{d0}) + [P_{\alpha r}^{INT} + 0]N_d(r_{d0})$ (with $N_{\alpha+\alpha r}^{eff}$ for $\delta < r_{d0}$+0.1 μm that of "SURF") is calculated, then $K_{\alpha,\alpha r}$ with $n_\alpha = 2$ and $n_{\alpha r} = 1$ and equally shifted by −14.6 and n_α adjusted to produce Fig. 13(b), again yielding a truncated α response distribution promoted above the neutron recoil distribution by a distance in agreement with Fig. 16(d) of Ref. [1] with $n_\alpha = 2.3$.

4.1.3. Proto-bubble multiplicity

The α response in Fig. 13(b) above the gap is problematic, with experiment indicating significantly higher K_α. These events however correspond to the larger r_{d0} in the DSD, for which the probability of a constant n_α is likely incorrect given Fig. 2(a). This was explored by incrementally increasing the $n_\alpha(r_{d0} > r_{gap})$ to obtain agreement with the experimental data, yielding the additional curve in each of the Figures. Fitting of the resulting $n_\alpha(r_{d0})$ yields Boltzmann distributions for each n_α as seen in Fig. 14.

Also note that $<N_{nr}^{eff}>$ in Fig. 13(a) occurs at a higher $\ln(K_{nr})$ than in Fig. 13(b) for which $<N_d>$is larger. This results from the difference in microphone distance (R^{-2} in Eqs. ((16) and (17)) of the two $\ln(A_m^2)$, which represents a ~ 20% increase in microphone distance : $\ln(A_m^2)|_{\text{Fig 13(a)}}$ - $\ln(A_m^2)|_{\text{Fig 13(b)}} = 1.4$ vs. the observed 1.5. In contrast, the $<N_\alpha^{eff}>$ of both Figs. remains at roughly the same $\ln(K_\alpha)$: this is also because of the R^{-2} difference, but mitigated by the difference in the DSD and P_α for which $r_{d0} < 10\,\mu$m do not participate in Fig. 13(a) and $r_{d0} < 40\,\mu$m do not participate in Fig. 13(b).

4.2. Application : PICASSO

The PICASSO science SDDs were 4.5 liter (14 cm Ø, 40 cm height) containing C_4F_{10} dispersed as a Gaussian DSD with a stated $N_d(<r_{d0}>,\Sigma) \sim N_d(100\,\mu m,\ 32\,\mu m)$ [3]. Neutron irradiations were performed with weak sources of AmBe, AcBe or low energy, monoenergetic neutron beams [3, 15]. Alpha irradiations were effected by doping the SDDs with an aqueous solution of ^{241}AmCl and/or ^{226}RaCl, using two smaller version SDDs (14 cm Ø, 13 cm height) of its standard devices (it isn't clear if the large volume DSDs suffered reduction in the smaller device fabrications). The SDDs were operated between 20 – 50ºC at 1 bar [3, 4, 15].

Each PICASSO SDD employed a set of 9 high frequency piezos (< 150 kHz), mounted external to the SDD containment in sets of 3 at three different heights, with sensitivity of $\vartheta = 27$ μV/μbar, signal amplification of 3000 and Bessel bandpass with cutoff below 18 kHz [3, 4]; the calibration SDDs, 3 piezos with 120º separation at the same height. Signal analysis, based on the acoustic energy of a recorded event, consisted of squaring the waveform of each transducer signal and integrating over its duration (~ 20.5 ms); the results were then averaged over all piezos for each event, and displayed as $N_{events}(AP)$ vs. $AP = \log\langle\int_0^\tau A^2 dt\rangle$, normalized such that the mean of the neutron recoil distribution was at AP = 1. The frequency cutoff increased from 18 kHz at the lower temperatures to 100 kHz at the highest in optimizing the gap between neutron- and α-generated events [15].

In this case, the signal obtains from the full droplet expansion, and the abscissa is then given by:

$$(\mathrm{AP})_j = \log\left(A_m^2 r_{d0}^6 n_j^3\right) \tag{22}$$

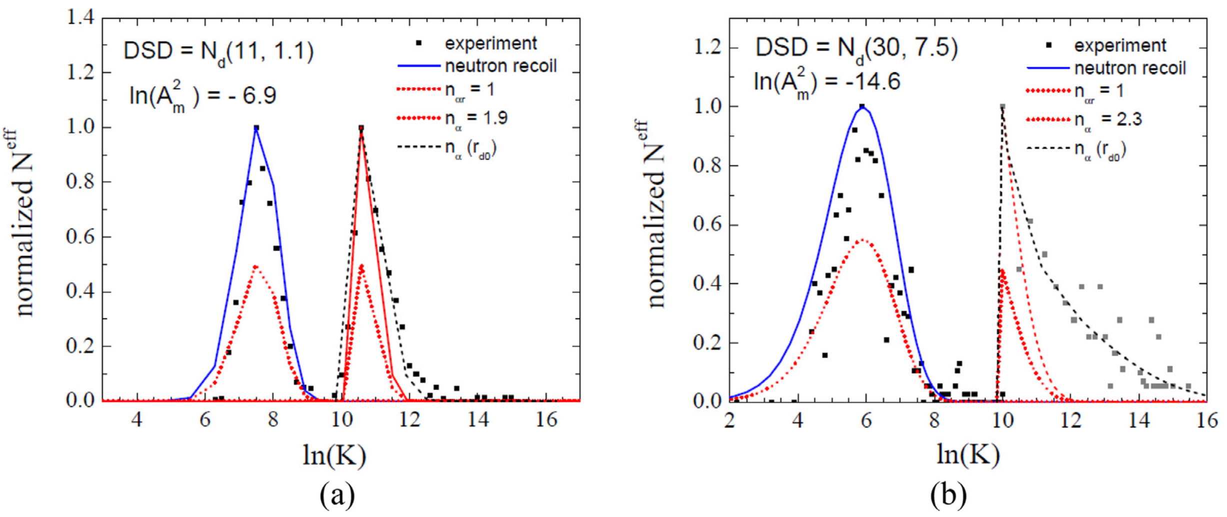

Fig. 13. (a) model results for SIMPLE with $E_\alpha = 4.2$ MeV and a Gaussian DSD of N_d(11 μm, 1.1 μm), and shift of -6.9 in both power spectra to account for the $\ln(A_m^2)$; (b) same for a Gaussian DSD with N_d(30 μm, 7.5 μm) and $E_\alpha = 5.6$ MeV, with a shift of -14.6 in both power spectra. The additional curve (black) in each panel portrays the change induced by an increasing proto-bubble generation rate by α above the r_{d0} of the gap onset.

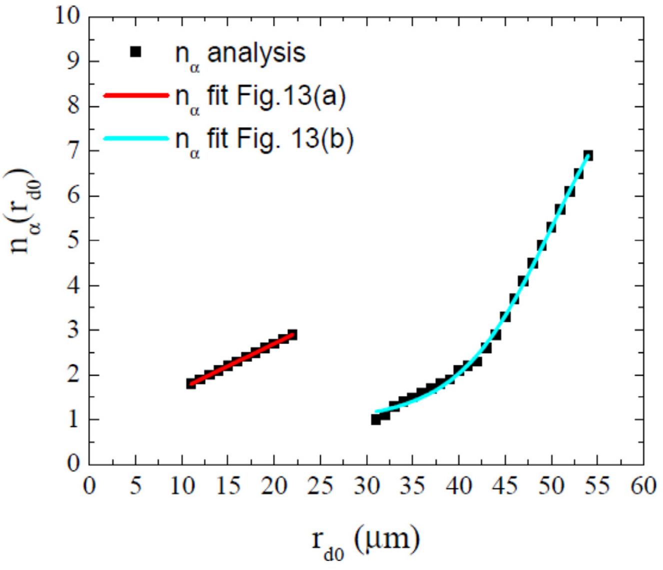

Fig. 14. variation in $n_\alpha(r_{d0})$ with r_{d0} used in adjusting Fig. 13. The lines indicate their Boltzmann fittings.

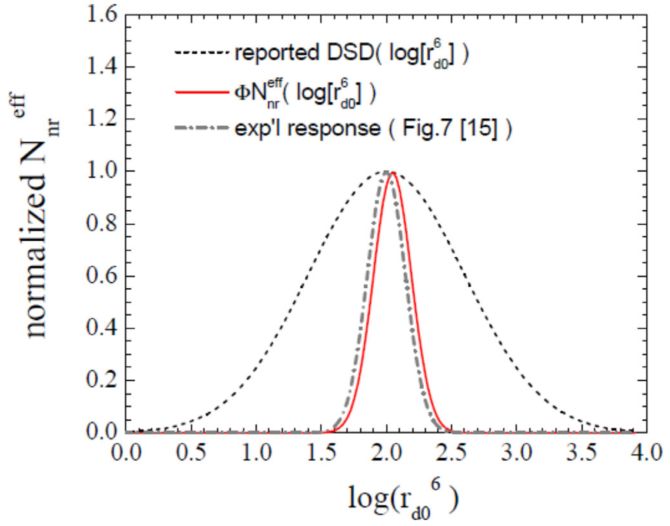

Fig. 15. comparison of the PICASSO N_{nr}^{eff} with the reported acoustic response (Fig. 7 [15]), and with ΦN_{nr}^{eff} with an offset of 0.05 for visibility (35ºC/1 bar).

where $r_d = (\frac{\rho_v}{\rho_\ell})^{1/3} r_{d0}$ and all constant factors are again subsumed into A_m^2.

4.2.1. Neutron calibrations

In contrast to the SIMPLE N_{nr}^{eff}, the PICASSO N_{nr}^{eff} unexpected appears in severe disagreement with its neutron irradiation response of Fig. 7 [15]. The model however does not account for the signal processing (filtering, amplification, squaring and integration, and averaging) in obtaining AP; which is seen in Ref. [15] to yield a response Gaussian with FWHM resolution of ~ 20%. To account for this, we adopt a transfer function (Φ) for the measurements, $N_{nr}^{eff} = \Phi \times P_j N_d$. Since both N_{nr}^{eff} and N_d are Gaussian, $\Phi = e^{-\frac{(AP - <AP>)^2}{2\Sigma^2}} = e^{-\frac{(AP - <AP>)^2}{2(0.489)^2}}$, which is applied to the N_j^{eff} after conversion of the representation from r_d to AP (see Fig. 15)

4.2.2. ^{241}Am calibrations

For the ^{241}Am calibrations, the N_{nr}^{eff} was calculated with $n_{nr} = 1$, then shifted by -10.5 to overlap the experimental acoustic neutron recoil distribution, and Φ applied. For the α-response, the $N_{\alpha+\alpha r}^{eff} = P_{\alpha r+\alpha}^{SURF} N_d$ was calculated with $p_\alpha = 32\,\mu$m by interpolation of Fig. 2(b), and $(AP)_{\alpha+\alpha r}$ computed with $n_\alpha = n_{\alpha r} = 1$ following Ref. [3], equally shifted by -10.5, and Φ applied. The result is shown in Fig. 16 for comparison with Fig. 10 of Ref. [15]. At 27 ºC, the SDD is only marginally sensitive to α's, and the α decay signal derives from either the α recoil or α (each with $n_j = 1$). From inspection of Figs. 6-8, the P_α^{SURF} contour traverses the DSD, previsioning no significant alteration of the N_α^{eff} response distribution relative to the N_{nr}^{eff} as in the case of SIMPLE.

4.2.3. ^{226}Ra calibrations

For the ^{226}Ra calibration results of Fig. 8 in Ref. [15], in which ^{226}Ra α-emitters were injected and allowed to diffuse throughout the SDD volumes, the analysis is a bit more complicated given the temperature variation of the measurements. The increase in AP of the recoil distribution with temperature follows from the increasing expansion velocity $(\frac{2}{3\rho_\ell}\Delta P)^3$ of Eq. (10) with temperature, as seen by the agreement between Col. 2 and Col. 4 of Table 3.

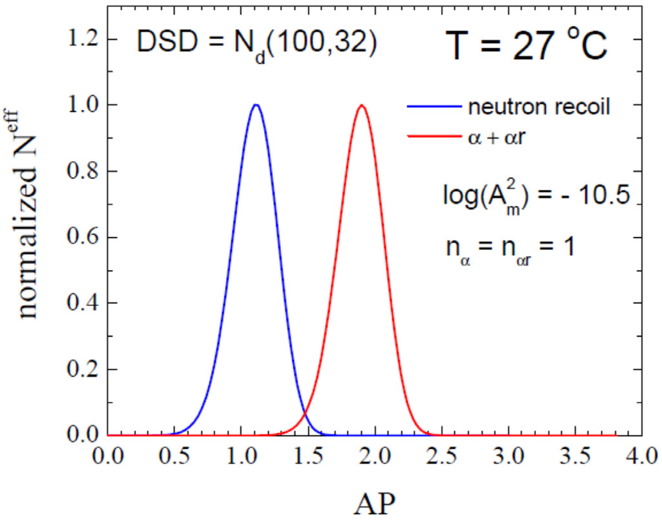

Fig. 16. (a) model results for PICASSO with N_d(100 μm, 32 μm), $E_\alpha = 5.4$ MeV, and shift of -10.5 in both acoustic energy responses to account for the log(A_m^2), and Φ application. The blue [base $(AP)_{nr}$] and red $(AP)_{\alpha+\alpha r}$ contours overlap.

Table 3
Comparison of reported nuclear recoil peak means (Figs. 8 of Ref. [15]) with normalized calculations of inertial velocity in the bubble expansion of C_4F_{10}.

T (ºC)	$(AP)_{nr}$ (Fig. 8 [15])	Log$(\frac{2}{3\rho_\ell}\Delta P)^3$	Col. 3 – (4.64)
25	1.0	5.64	1.0
27	1.5	6.05	1.4
35	1.8	6.28	1.6
45	2.3	6.82	2.2

Table 4
Comparison of fit values for $q_{\alpha r}$ and q_α with those reported in Fig. 9 of Ref. [15].

T (ºC)	$q_{\alpha r}$ (fit)	$q_{\alpha r}$ (Fig. 9 [15])	q_α (fit)	q_α (Fig. 9 [15])
25	0.99	0.97	0.01	0.03
27	0.70	0.40	0.30	0.60
35	0.19	0.20	0.81	0.80
45	0.04	0.03	0.96	0.97

The ^{226}Ra decay is –($t_{1/2} = 1600$ y)-> 4.87 MeV $\alpha + {}^{222}$Rn [19]. At 25 ºC the SDD is insensitive to the decay α's since the E_α are well below the α threshold. The $p_{\alpha,\alpha r}$(T) were obtained by interpolation of Fig. 2(b) and the computed ^{222}Rn α Bragg curve, adopting $E_\alpha = 5.6$ MeV of the ^{222}Rn decay.

The approach is otherwise the same: the N_{nr}^{eff} is shifted by -10.5 to overlap the experimental result, and Φ applied. The $N_{\alpha+\alpha r}^{eff} = q_\alpha P_{\alpha r+\alpha}^{INT} N_d + q_{\alpha r} P_{\alpha+\alpha r}^{EXT} N_d$ was initially calculated by adjusting the respective q_j to reproduce the contours of the Figs. 8 [15] response, and afterwards the q_j's compared with Fig. 9 [15]: as seen in Table 4, with the exception of the $T = 27$ ºC entry, the q_j(T) at each temperature are seen to be in reasonable agreement, the discrepancy possibly being the result of the steep slopes of the α and α recoil contours which cross at this point in the Figure.

The $(AP)_{\alpha,\alpha r}$ was then computed with $n_\alpha = n_{\alpha r} = 1$ following Ref. [15], equally shifted by -10.5, and Φ applied to both distributions. Figs. 17 show the resulting particle responses corresponding to Figs. 8 of Ref. [15], for comparison.

Again, the most obvious effect of the model, from inspection of Figs. 6–8, is that all of the P_α^k contours sample the entire DSD, previsioning no significant alteration of the N_α^{eff} response relative to the N_{nr}^{eff} as in the case of SIMPLE. The nr- and (α+αr)-distributions overlap at least partially at all temperatures, in agreement with Ref. [15]. In Fig. 17(a), the E_α is below the α sensitivity threshold: the neutron recoil and α recoil responses superimpose. With temperature increase, the E_c decreases and the SDD is increasingly responsive to the α, which combines with its daughter recoil response to yield the almost single α+αr acoustic peak in Fig. 17(d).

5. Discussion & conclusions

The results of Section 4 clearly demonstrate the role of the detector DSD in both the selection of interaction events to be detected, and their associated acoustic signatures. The neutron response (N_{nr}^{eff}) is essentially a projection of the DSD and can be used in SDD calibrations as a non-invasive measurement of the DSD and identification of any transfer function. The α response (N_α^{eff}) in contrast reflects the location of the α-emission with respect to the DSD droplets: those of $r_{d0} \leq p_\alpha/2$ are insensitive to internal and surface α emissions, yielding an asymmetric N_α^{eff} which may be gapped from that of the N_{nr}^{eff} depending on the number of proto-bubbles generated by the α energy loss.

The use of large droplets, as pursued by PICASSO [40] in order to fully contain the α decay, together with the C_4F_{10} and its high LET$_c$ relative to the α Bragg peaks, is seen to be counter-productive since these preclude the asymmetry in $N_\alpha^{eff}$from which the gap with N_{nr}^{eff} in SIMPLE arises.

The small droplets are however fully sensitive to the accompanying α recoil events ($N_{\alpha r}^{eff}$), providing a background to the N_{nr}^{eff}since both n_j=1: The presence of radon and its decay daughters in the U/Th decay chains and their apparent diffusion into the droplets [15] remains a serious problem in SDD dark matter experiments (as well as any application requiring neutron-α discrimination), since these mimic the recoil of target nuclei. Minimization of U/Th contaminants in the SDD construction materials continues to be required, and further investigation is required of the electrochemical properties of the decay daughters, and their diffusion in the SDD gel and liquid media.

The analysis is rudimentary by design, neglecting or simplifying a number of details in both the particle interaction and acoustic response descriptions. In the first case, this includes ion straggling, nucleation efficiencies, uncertainties in the p_j because of the track length averaging of particle trajectories in constructing the Bragg curves, use of $\rho_{gel} = \rho_\ell$ in the PICASSO application (the Bragg peaks in the gel are generally shifted to smaller depths than in the superheated liquid itself), inter-droplet distance effects, and the distances of α travel in the liquids. The acoustic response, in turn, includes various simplifications of the Rayleigh-Plesset [24] and Plesset-Zwick [25] equations in obtaining the solutions (neglect of viscosity, time-dependent surface tension, thermal conductivities), and is restricted to spherical droplets/bubbles.

The analysis presented is moreover fundamentally based on knowledge of the particle p_j in the target liquid, which is defined by the LET$_c$ and hence the Λ - which is seen in Section 2.1 not to be well-defined. The LET$_c$ provides only the p_j: although the particle dE/dx along its trajectory, at least in the case of SIMPLE, differentially exceeds the LET$_c$ over several micron, theory does not address the number of proto-bubbles formed per unit distance in the ion passage. Recent molecular simulations for C_2ClF_5 [41] obtain in the case of SIMPLE $n_\alpha \sim 5$ proto-bubbles per micron of liquid penetration above p_α, which is larger than the $n_\alpha \sim 2$ obtained here initially. The Boltzmann increase in n_α with increasing r_{d0} identified in Section 4 is qualitatively consistent with the contour of the leading edge Bragg peak above LET_c, suggesting a physical basis for its implementation. Inclusion of the $p_>$ in an analogue analysis, and comparison of the two results with experiment, may provide additional information on this question.

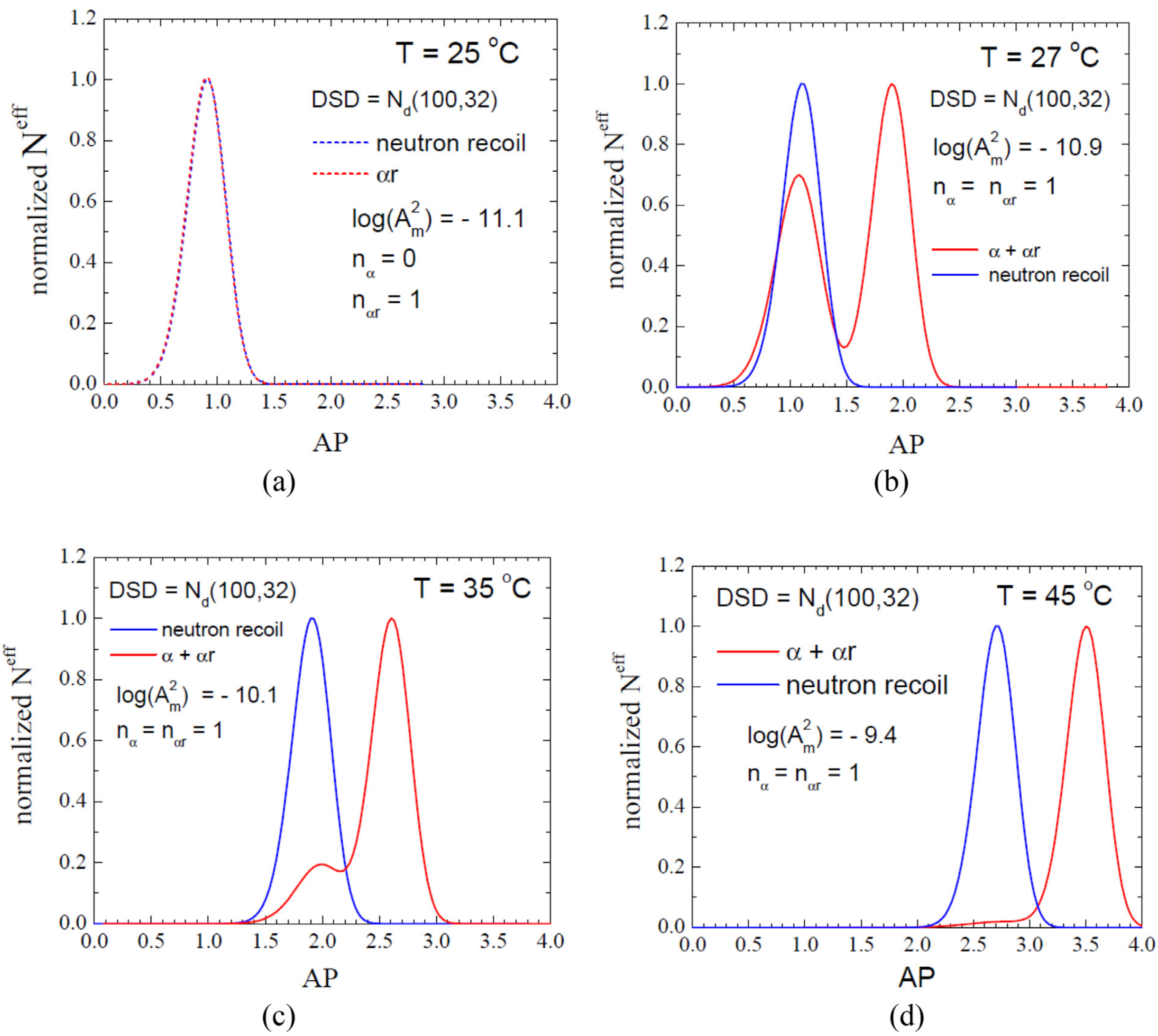

(a) (b)

(c) (d)

Fig. 17. model results for comparison with Figs. 8 of Ref. [15], including the shift of log(A_m^2) in both and Φ application, which decrease with increasing temperature owing to ρ_ℓ(T) and c(T). The blue contours are $(AP)_{nr}$; the red curves display $(AP)_{\alpha+\alpha r}$.

Recent similar molecular simulations for the case of a C_3F_8 bubble chamber [42] have more recently examined the acoustic signal production, however focusing on the early-time proto-bubble generation, and providing important quantifications of the "heat spike"-to-proto-bubble evolution. They however observe that only a single proto-bubble is nucleated per α in the $^{222}\text{Rn} \rightarrow {}^{210}\text{Pb}$ decay chain. Evaluation of the involved acoustic energies via Eq. (17) yields larger signal amplitudes than those induced by neutron-generated recoils.

Proto-bubble nucleation by electrons has also been recently examined in C_3F_8 bubble chambers [43], in which experimental data is found to be in better agreement with a new nucleation mechanism for which the energy threshold contains only the first and last terms of Eq. (1), and the E_c in the nucleation probability is replaced by -Λ. The γ calibration data in CF3I chambers are however seen to agree with Seitz, as a result of Auger cascades in the high-Z atoms which produce a more local energy deposition. In short, significant further investigations of the involved molecular dynamics, and interactions with particles other than neutrons and α's, are required to further reveal the underlying physics and elucidate the full discrimination details.

The analysis presented herein, as simplified as it is, nevertheless appears to capture the essence of the involved particle response physics, and provide a basis for understanding the differences in neutron - α particle discrimination capacities of the SDD devices. The results remove the disagreement between the SIMPLE and PICASSO experiments with respect to their respective particle discrimination, demonstrating that each of the observed responses is obtained with the respectively stated DSDs and measurement conditions. The reduced discrimination of PICASSO is seen to arise from the broad distribution of larger droplet sizes, which are fully sampled by the nucleation probabilities P_α^k necessary to proto-bubble nucleation, leading to an apparent droplet size-independence of the SDD response. The smaller, narrower DSDs of SIMPLE are in contrast partially unsampled by the P_α^k, which is manifested in an asymmetric α response which provides the gap.

Both SIMPLE and PICASSO have evolved to bubble chambers in the search for astroparticle dark matter. While the basic physics outlined above remains operative, the case of bubble chambers is simpler since neither DSD nor gel matrix are involved, obviating the droplet p_j cutoff considerations of Section 3: any α event includes both the α and α daughter contributions with $\sim$ 100% probability, so long as both satisfy Eqs. (1) and (2), and the decay occurs at a sufficiently large distance from the containment walls. The results herein nevertheless remain important in providing further guidance to the continued development of SDD applications. Neutron irradiations and precise knowledge of both the DSD and LET_c constitute important ingredients of a standard calibration from which the detector response can be projected.

Declaration of Competing Interest

The authors declare that they have no known competing financial interests or personal relationships that could have appeared to influence the work reported in this paper.

Acknowledgements

This work was funded in part by the former Nuclear Physics Center of the University of Lisbon, and by the Portuguese Foundation for Science and Technology (FCT) via grants PTDC/FIS/115733/2009 and PTDC/FIS/121130/2010. The activities of Felizardo and Fernandes are supported by FCT (grant SFRH/BPD/94028/2013 and contract IF/00628/2012/CP0171/CT0008, respectively); those of Morlat by FCT (grant UID/Multi/04349/2013). Additional FCT support through project grant PTDC/EEI-ELC/2468/2014 is gratefully acknowledged, as also the participation of Prof. J. Antunes, and MSc's Marta Reis and Filipe Soares in various aspects of this investigation.

References

[1] M. Felizardo, TA Girard, T. Morlat, et al., (The SIMPLE Collaboration), Phase II of the SIMPLE dark matter search, Phys. Rev. D89 (2014) 072013.
[2] M. Felizardo, T. Morlat, TA Girard, A. Kling, A.C. Fernandes, J.G. Marques, F. Carvalho, A.R. Ramos, Neutron - alpha irradiation response of superheated emulsion detectors, Nucl. Instr. Meth. A863 (2017) 62.
[3] E. Behnke, M. Besnier, P. Bhattacharjee, X. Dai, et al., Final results of the PICASSO dark matter search experiment, Astroparticle Physics 90 (2017) 85.
[4] S. Archambault, et al., Constraints on low-mass WIMP interactions on ^{19}F from PICASSO, Phys. Lett. B711 (2012) 153.
[5] A.C. Kamaha, Improved limits on the existence of dark matter: the final results from the PICASSO experiment PhD Thesis, Queen's University, Canada, 2015.
[6] M. Fínes-Neuschild, Étude et caracterisation de détecteurs à liquide en surchauffe MSc Thesis, University of Montreal, Canada, 2014.
[7] F. Seitz, On the theory of the bubble chamber, Phys. Fluids 1 (1958) 2.
[8] F. d'Errico, Radiation dosimetry and spectrometry with superheated emulsions, Nucl. Instrum. Meth. B184 (2001) 229.
[9] M. Das, T. Sawamura, Estimation of nucleation parameter for neutron-induced nucleation in superheated emulsion, Nucl. Instrum. Meth. A531 (2004) 577.
[10] S. Seth, M. Das, S. Bhattacharya, P. Bhattacharjee, S. Saha, The nucleation parameter for heavy-ion induced bubble nucleation in superheated emulsion detector, Journ. Instrumentation 8 (2013) P05001.
[11] NIST, REFPROP code, NIST Standard Database 23, V.7 (2002).
[12] C.L. Yaws, M.A. Satyro, Enthalpy of vaporization-organic compounds, in: C.L. Yaws (Ed.), Thermophysical properties of chemicals and hydrocarbons, William Andrew Publishing, Norwich, NY, 2009, pp. 309–400. (Chapter 7).
[13] M. Das, Searching for universal behaviour in superheated droplet detector with effective recoil nuclei, Pramana 80 (2013) 994.
[14] E. Behnke, J.I. Collar, P.S. Cooper, K. Crum, M. Crisler, et al., Spin-dependent WIMP limits from a bubble chamber, Science 319 (2008) 933.
[15] S. Archambault, et al., New insights into particle detection with superheated liquids, New Journ. Phys. 13 (2011) 043006.
[16] F. Giuliani, J.I. Collar, D. Limagne, T. Morlat, J.G. Marques, C. Oliveira, TA Girard, G. Waysand, Response of SIMPLE SDDs to monochromatic neutron irradiations, Nucl. Instrum. Meth. A526 (2004) 348.
[17] A.C. Fernandes, A. Kling, M. Felizardo, T.A. Girard, A.R. Ramos, J.G. Marques, M.I. Prudêncio, R. Marques, F.P. Carvalho, I. Lázaro, Neutron background signal in superheated droplet detectors of the Phase II SIMPLE dark matter search, Astrop. Phys. 76 (2016) 48.
[18] J.F. Ziegler, M.D. Ziegler, J.P. Biersack, SRIM – The stopping and range of ions in matter (2010), Nucl. Instr. Meth. B 268 (2010) 1818.
[19] R.B. Firestone, V.S. Shirley, C.M. Baglin, S.Y.F. Chu, J. Zipkin (Eds.), Table of isotopes, John Wiley & Sons Inc, 1976.
[20] G.F. Knoll, Radiation detection and measurement, John Wiley & Sons, NY, 1989.
[21] L.K. Pan, C.-K.C. Wang, Superheated-liquid-droplet technique for measuring alpha decays in uranium solutions, Nucl. Instrum. Meth. A420 (1999) 345.
[22] J.E. Grindler, The radiochemistry of uranium, (National Academy of Science-National Research Council, Washington, 1962); P.A.G. OÕhare, E.H.P. Cordfunke, The chemical thermodynamics of actinide elements and compounds, Part 3 Miscellaneous actinide compounds (International Atomic Energy Agency, Vienna, 1978).
[23] M. Felizardo, T. Morlat, J.G. Marques, A.R. Ramos, TA Girard, A.C. Fernandes, A. Kling, I. Lázaro, R.C. Martins, J. Puibasset, (SIMPLE Collaboration), Fabrication and response of high concentration SIMPLE superheated droplet detectors with different liquids, Astroparticle Physics 49 (2013) 28.
[24] L. Rayleigh, On the pressure developed in a liquid during the collapse of a spherical cavity, Phil. Mag. 34 (1917) 94 M.S. Plesset, The dynamics of cavitation bubbles, ASME J. Appl. Mech. 16 (1949) 228.
[25] M.S. Plesset, S.A. Zwick, The growth of vapor bubbles in superheated liquids, J. Appl. Phys. 25 (1954) 493.
[26] H.-Y. Kwak, S.D. Oh, C.-H. Park, Bubble dynamics on the evolving bubble formed from the droplet at the limit of superheat, Int. J. Heat Mass Transfer 38 (1995) 1709.
[27] K.-T.Byun H.-C.Park, H.-Y. Kwak, Explosive boiling of liquid droplets at their superheat limits, Chemical Engineering Science 60 (2005) 1809.
[28] S.A Glaser, D.C. Rahm, Characteristics of bubble chambers, Phys. Rev. 97 (1955) 474.
[29] Yu.A. Alexsandrov, G.S. Voronov, V.M Gorbunkov, N.B. Delone, Yu.I. Nediayov, Bubble Chambers, Indiana University Press, Bloomington and London, 1967.
[30] Ch. Peyrou, Bubble chamber principles, in: R.P. Shutt (Ed.), Bubble and Spark Chambers, 1, Academic Press, New York, 1967.
[31] J.E. Shepherd, Dynamics of vapor explosions: rapid evaporation and instability of butane exploding at the superheat limit PhD Thesis, California Institute of Technology, 1981, p. 159.
[32] A. Prosperetti, Vapor bubbles, Ann. Rev. Fluid Mech 49 (2017) 221.
[33] Ethermo calculation platform, Thermodynamics & transport properties, www.ethermo.us, 2020.
[34] A.J. Robinson, R.L. Judd, The dynamics of spherical bubble growth, Int. J. Heat Mass Transfer 47 (2004) 5101.
[35] B.B. Mikic, W.M. Rohsenow, P. Griffith, On bubble growth rates, Int. J. Heat Mass Transfer 13 (1970) 657.
[36] M. Minnaert, On musical air-bubbles and the sounds of running water, Phil. Mag. 16 (1933) 235.
[37] Yu.N. Martynyuk, N.S. Smirnov, Sound generation in superheated liquids by heavy charged particles, Sov. Phys. Acoust. 37 (1991) 376.
[38] A. Zhao, S. Glod, D. Poulikakos, Pressure and power generation during explosive vaporization on a thin-film microheater, Int'l. Journ. of Heat and Mass Transfer 43 (2000) 281.
[39] L. Kinsler, A Frey, A. Coppens, J. Sanders, Fundamentals of acoustics, John Wiley & Sons, Inc., New York, 2000.
[40] F. Aubin, M. Auger, M.H. Genest, G. Giroux, et al., Discrimination of nuclear recoils from alpha particles with superheated liquids, New J. Phys. 10 (2008) 103017.
[41] P. Denzel, J. Diemand, R. Angélil, Molecular dynamics simulations of bubble nucleation in dark matter detectors, Phys. Rev. E93 (2016) 013301.
[42] T. Kozynets, S. Fallows, C.B. Krauss, Modeling emission of acoustic energy during bubble expansion in PICO bubble chambers, Phys. Rev. D100 (2019) 052001.
[43] C. Amole, M. Ardid, I.J. Arnquist, D.M. Asner, et al., Data-driven modeling of electron recoil nucleation in PICO C_3F_8 bubble chambers, Phys. Rev. D100 (2019) 082006.